
Co-folding model guided by structural proteomics

Alon Shtrikman^{1*} Nitzan Simchi^{1*} Michal Ran Shchory^{1*}
Sagie Brodsky^{1*} Eran Seger¹ Kirill Pevzner^{1✉}

¹Protai Bio
kirill@protai.bio

*Equal Contribution ✉Corresponding Author

Abstract

Protein structure generative models excel at predicting single protein static structures from sequence, but routinely fail to capture the correct conformational state of protein complexes, critical for protein design and induced proximity modalities such as antibodies and PROTACs. While structural proteomics techniques like Cross-Linking Mass Spectrometry (XL-MS) and Hydrogen-Deuterium Exchange (HDX-MS) offer valuable spatial and dynamic insights, integrating these sparse, heterogeneous measurements into these models remains an open challenge. Here, we bridge this gap by combining structural proteomics data with the rich biophysical priors learned by pretrained diffusion models. We introduce AIMS-Fold, an inference-time guided-diffusion framework that actively steers the generative sampling trajectory using differentiable physical potentials derived from XL-MS spatial restraints and HDX-MS solvent accessibility profiles. We demonstrate that these structural methods individually enhance predictive accuracy, and their integration yields synergistic improvement. Crucially, by leveraging these experimental restraints, AIMS-Fold achieves higher accuracy on challenging induced proximity targets than purely computational, unguided state-of-the-art models like Boltz-2. This establishes our framework as a powerful, integrative computational approach for the structure based drug design of induced proximity drugs. Evaluation code will be made publicly available upon publication.

1 Introduction

Proximity-inducing drugs, including proteolysis-targeting chimeras (PROTACs) and molecular glues, represent a new class of therapeutic modalities[1, 2]. Unlike classical small molecule inhibitors whose efficacy is dictated by the binary binding affinity to a single target, the activity of proximity inducers is driven by the assembly and dynamic behavior of a ternary complex (e.g., a target protein, the bridging molecule, and an effector like an E3 ligase)[3–6]. For rational drug design, using the correct protein complex state is critical[7]. These complexes require a balance between structural stability and the flexibility to execute biological functions, such as optimal ubiquitination geometry[8, 9].

Recently, sequence-to-structure deep learning models, most notably AlphaFold3[10] and Boltz-2[11], have impacted structural biology by providing highly accurate proteome-wide structure predictions. Despite these breakthroughs, such models are predominantly trained to map a sequence to a single, static structural state[12]. Since dynamic protein-protein interactions and drug-induced complexes are sparsely represented in training repositories like the Protein Data Bank (PDB), these models

frequently suffer from overconfidence in predicting one static state[13]. Consequently, they fail to capture the conformational shifts driven by induced proximity drugs[14, 15].

Structural proteomics solves this by capturing the dynamics of protein complexes[16]. Cross-linking mass spectrometry (XL-MS) provides spatial constraints[13, 16], while hydrogen-deuterium exchange (HDX-MS) captures solvent accessibility[17]. Integrating raw MS data directly into structure generative models to actively guide structure prediction remains a challenge[18].

In this work, we bridge this gap by introducing AIMS-Fold, a novel diffusion-based generative model that actively uses sparse structural proteomics data to guide structure generation. Rather than relying on model weights alone for static structure predictions or post-hoc filtering using experimental data[19–21], AIMS-Fold applies inference-time steering[22] to a pretrained atomic diffusion model. By translating XL-MS and HDX-MS data into differentiable physical potentials, our method actively alters the probability landscape during the reverse diffusion process, guiding the sampling trajectory toward biologically compatible conformations that satisfy the experimental constraints. We demonstrate that integrating positive and negative spatial restraints (XL-MS) with solvent accessibility patterns (HDX-MS) yields significantly improved performance compared to unconstrained generation or post-hoc filtering.

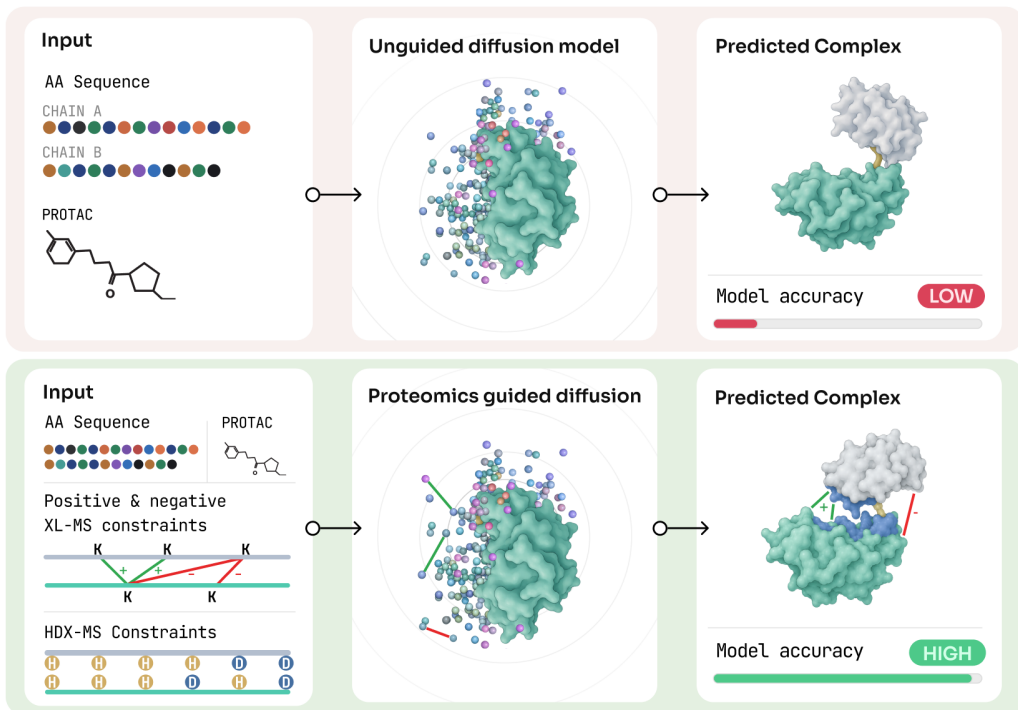


Figure 1: AIMS-Fold is an inference-time guided-diffusion framework that actively steers the generative sampling trajectory using experimentally derived constraints. While Boltz-2 inputs mainly include SMILES and protein sequences, AIMS-Fold receives HDX-MS, XL-MS positive and XL-MS negative constraints to improve model prediction accuracy.

2 Background

2.1 Diffusion-based structure generation

Recent advances in biomolecular modeling, such as AlphaFold3[10] and Boltz-2[11], frame structure prediction as a continuous-time generative diffusion process. The model operates directly in the space of 3D atomic coordinates, where a protein structure of N atoms is represented as $\mathbf{x} \in \mathbb{R}^{N \times 3}$.

The forward diffusion process gradually noises the data $\mathbf{x}_0 \sim p_{\text{data}}$ into a standard Gaussian distribution over a time variable $t \in [0, T]$. This destruction of signal is governed by a stochastic differential equation (SDE)[23]:

$$d\mathbf{x} = f(\mathbf{x}, t)dt + g(t)d\mathbf{w} \quad (1)$$

In this formulation, the drift and diffusion coefficients are denoted by $f(\mathbf{x}, t)$ and $g(t)$, respectively, while $d\mathbf{w}$ characterizes a standard Wiener process.

To sample from the target distribution and generate novel structures, the model samples pure noise $\mathbf{x}_T \sim \mathcal{N}(0, \mathbf{I})$ and simulates the reverse-time SDE (reverse diffusion process)[23, 24]:

$$d\mathbf{x} = [f(\mathbf{x}, t) - g(t)^2 \nabla_{\mathbf{x}} \log p_t(\mathbf{x})] dt + g(t)d\bar{\mathbf{w}} \quad (2)$$

Because the true marginal score function $\nabla_{\mathbf{x}} \log p_t(\mathbf{x})$ is intractable, a neural network $s_{\theta}(\mathbf{x}, t)$ is trained via denoising score matching[25] to approximate it. At each sampling timestep, the model predicts the fully denoised ground-truth structure, denoted as $\hat{\mathbf{x}}_0(\mathbf{x}, t)$, which drives the trajectory toward a folded protein state.

2.2 Inference-time steering via energy potentials

A major innovation integrated into Boltz-2 is the steering mechanism, an inference-time method that applies physics-based potentials to correct non-physical predictions and guide the model toward specific conformational basins. Crucially, this alters the probability landscape without requiring any retraining of the base neural network. Mathematically, a differentiable energy potential $U(\mathbf{x})$ is defined to represent the desired structural constraint. Using Tweedie’s formula[26, 22], the potential is evaluated on the network’s current denoised prediction $\hat{\mathbf{x}}_0(\mathbf{x}, t)$. The gradient of this potential is then injected directly into the score function to guide the sampling trajectory[22]:

$$\tilde{s}_{\theta}(\mathbf{x}, t) = s_{\theta}(\mathbf{x}, t) - \lambda(t) \nabla_{\mathbf{x}} U(\hat{\mathbf{x}}_0(\mathbf{x}, t)) \quad (3)$$

where $\lambda(t)$ is a time-dependent scaling factor that dictates the strength of the guidance. Boltz-steering utilizes flat-bottomed penalty functions. This means the potential applies zero gradient penalty as long as the generated structure satisfies the condition, but applies an increasingly severe penalty when boundaries are violated. Natively, Boltz utilizes this mechanism to enforce physical plausibility, applying potentials to resolve steric clashes and correct stereochemistry errors during the generation.

3 Methods

3.1 MS-guided diffusion and steering

AIMS-Fold is a diffusion-based generative model for biomolecular structure prediction built upon the Boltz-2 architecture[11]. This work uses and extends the Boltz-2 implementation, available under the MIT License. To better support structural proteomics constraints, we extend inference time guidance (Boltz Steering) to steer the generation process toward biologically compatible geometries. Rather than relying solely on the neural network to predict the denoising step, AIMS-Fold calculates energy potentials based on intermediate atomic coordinates. The gradients of these physics-informed potentials are injected into the sampling trajectory[22], actively altering the probability landscape to guide the model into conformational basins that satisfy experimental data.

3.2 XL-MS distance guidance and negative constraints

Following standard quality control and normalization, XL-MS data is incorporated as distance constraints. Cross-links identified by XL-MS yield two types of spatial constraints: positive constraints, which dictate that target residues reside within a specified proximity distance under a given experimental condition, and negative constraints, which infer that the residues distance exceeds the physical

reach of the cross-linker. For positive constraints, we utilize the existing Boltz-2 distance potentials to attract specified residues.

Crucially, XL-MS data derived from differential experimental conditions can derive negative constraints (e.g., a cross-link present in multiple treatments but missing in a specific state). To support this, we introduce a negation flag that establishes a repulsive potential, pushing the specified residues beyond a user-defined distance threshold d_{\min} to satisfy the differential missing-link data. For a set of negatively constrained residue pairs \mathcal{N}_{neg} , the repulsive potential is formulated as:

$$U_{\text{neg}}(\mathbf{x}) = \sum_{(i,j) \in \mathcal{N}_{\text{neg}}} \max(0, d_{\min} - d_{ij})^2 \quad (4)$$

This applies a quadratic penalty only when the Euclidean distance d_{ij} falls below the required threshold, forcing the two residues apart during the reverse diffusion steps.

3.3 Integrating HDX-MS protection data

Hydrogen-deuterium exchange mass spectrometry (HDX-MS) captures proximate, dynamic physical interactions, such as interface flexibility, that standard spatial constraints cannot fully resolve[27]. Experimental HDX-MS relative fractional uptake values encode the difference in deuterium uptake between states, where negative values indicate protection upon complex formation. To translate these protection signals into active guidance during the diffusion process, AIMS-Fold employs two strategies: a distance proxy and a physically differentiable burial potential.

Distance-based proxy constraints We map protection data to spatial geometry. Each protected residue generates an independent contact constraint against all residues of the other chain. The maximum distance threshold is dynamically scaled by the magnitude of the experimental protection:

$$d_{\max}(i) = d_{\text{base}} (1 - |\Delta_i| w_s) \quad (5)$$

where $d_{\max}(i)$ is the adjusted maximum distance boundary for residue i , d_{base} is the default baseline interaction distance, $|\Delta_i|$ is the absolute magnitude of the experimental HDX-MS protection signal (derived from the relative fractional uptake difference, see subsections 3.5 and B.2), and w_s is a tunable scaling weight defining the sensitivity of the threshold to the experimental signal. This calculated threshold is clamped to a minimum of 3\AA . This formulation ensures that the spatial constraint remains proportional to the biological signal: residues exhibiting a large HDX-MS protection upon complex formation (a large $|\Delta_i|$) strictly shrink the $d_{\max}(i)$ boundary, receiving tighter distance bounds and forcing the model to bury them closer to the interaction interface during generation.

Differentiable SASA-based protection guidance To more directly model the HDX-MS protection solvent accessibility, we implement a differentiable burial potential. For each protected residue i , we compute a Gaussian-weighted neighbor count burial $_i$ as a differentiable proxy for Solvent Accessible Surface Area (SASA):

$$\text{burial}_i = \sum_{j \neq i} e^{-\frac{d_{ij}^2}{2\sigma^2}} \quad (6)$$

where d_{ij} is the distance between atoms, and σ is the width of the Gaussian kernel. A smaller σ yields a tighter burial definition, while a larger value provides a broader receptive field. The burial value is then converted to a pseudo-SASA metric by using an exponential decay function relative to a reference burial constant burial $_{\text{ref}}$:

$$\text{SASA}_i = e^{-\frac{\text{burial}_i}{\text{burial}_{\text{ref}}}} \quad (7)$$

For each experimentally protected residue i , a quadratic loss \mathcal{L}_i is applied if the SASA $_i$ exceeds the protection threshold τ :

$$\mathcal{L}_i = k \max(0, \text{SASA}_i - \tau)^2 \quad (8)$$

The total loss \mathcal{L} is the sum of these penalties:

$$\mathcal{L} = \sum_{i \in \text{protected}} \mathcal{L}_i \quad (9)$$

3.4 Guidance scheduling

To ensure that the injection of physical priors does not destabilize the protein folding, we employ a piecewise timestep schedule over the reverse diffusion trajectory, progressing from pure noise to a fully denoised structure. Applying strong guidance too early in the denoising process corrupts the generation, while applying it too late fails to influence the global topology. Because cross-linking mass spectrometry and hydrogen-deuterium exchange influence the structure at different spatial resolutions, we decouple their respective guidance schedules. Initially, the HDX-MS guidance is disabled when the structure is too noisy for solvent accessible surface area to be structurally meaningful. It is then applied to seed the burial of protected residues while the global fold remains highly fluid, and eventually ramps up to full strength to rigidly reinforce the experimental solvent accessibility profile as the global structure consolidates. Conversely, spatial constraints derived from cross-linking dictate the global arrangement of the complex. To allow the base model to first establish local secondary structures without interference, this spatial guidance is delayed and is applied more sparsely to optimize inference speed. It remains disabled during the initial unconstrained folding phase, is applied at a partial strength to gently draw the cross-linked domains toward each other, and reaches full strength only in the final stages of diffusion to stabilize the interaction interfaces and satisfy the rigid distance boundaries. Full timestep boundaries and hyperparameter configurations for these schedules are detailed in Appendix A.

3.5 Constraints derivation from raw data

To effectively guide the diffusion trajectory, raw mass spectrometry measurements must be translated into actionable constraints. We implemented processing pipelines for XL-MS and HDX-MS data, followed by an iterative subsetting strategy to resolve contradictory signals.

Cross-linking mass spectrometry constraints are derived directly from normalized, high-confidence MS intensity data. Positive constraints are assigned to residue pairs that exhibit significantly enriched intensity in the target biological state. Conversely, negative constraints are assigned to residue pairs that exhibit significantly lower intensity in one experimental condition compared to another. These act as repulsive spatial bounds, applying a gradient penalty to push the respective residues beyond the maximal physical length of the cross-linker. Hydrogen-deuterium exchange constraints are derived by comparing the fractional uptake between the protein complex and the isolated binary or apo states.

Because experimental MS data inherently contains noise, and because it captures dynamic ensembles where it is unknown a priori which specific constraints originate from the same discrete conformation, we implemented an iterative constraint subsetting strategy. Rather than applying all constraints simultaneously, the constraint pool is partitioned into numerous subsets. The model performs parallel guided generations across these subsets, and we assess constraint satisfaction for each resulting structure (more details in section 4.1). Subsets that yield high satisfaction rates are preserved and combined. This iterative process of generation, evaluation, and recombination effectively prunes noisy or contradictory signals, ultimately converging on a consistent constraint subset for the final, high-accuracy structure generation.

3.6 Related work

Historically, MS-derived experimental restraints have been integrated using docking and integrative modeling platforms such as HADDOCK[28], RosettaHDX[20], DOT2[21] and HDXRank[19]. These methods typically use XL-MS distance bounds and HDX-MS protection factors as scoring functions to filter and rank large number of generated candidate structures[29]. These approaches rely heavily

on rigid-body docking or limited flexible refinement and scale poorly for highly dynamic, multi-state complexes such as PROTAC ternary structures[1].

To bridge the gap between AI structure prediction and MS data, recent work has attempted to integrate experimental restraints directly into neural network architectures. AlphaLink1[30] and AlphaLink2[31] successfully integrate XL-MS data to improve the prediction of challenging protein-protein interactions and antibody-antigen complexes. However, these methods treat cross-links as explicit input features, requiring extensive retraining or fine-tuning of the underlying AlphaFold architecture (e.g., modifying the pair representation), which limits their flexibility. In contrast, AIMS-Fold requires no model retraining as it is an inference-time guidance method.

The concept of using a pretrained diffusion model as a structural regularizer for experimental data was recently demonstrated by CryoBoltz[32]. CryoBoltz applies inference-time guidance to Boltz-1, steering the sampling trajectory to minimize the distance between the predicted structure and a 3D point cloud representation of a cryo-EM density map.

4 Results

To evaluate AIMS-Fold, we conducted benchmarking across both synthetic and experimental datasets. Our evaluation framework is designed to first establish the MS-guided diffusion on clean cases where the data is ideal, followed by validation on noisy, heterogeneous experimental data captured from challenging induced proximity complexes. Furthermore, we evaluated our MS-guided generation against a post-hoc filtering approach, where dozens of unconstrained candidates are generated and subsequently ranked by their agreement with the structural MS data.

Table 1: Quantitative evaluation of AIMS-Fold and Boltz-2 (Unguided) on different cases. The table details the percentage of satisfied constraints, categorized by constraint type, for each evaluated case. To identify the best of 5 prediction, we ranked the generated models by the highest percentage of fulfilled experimental constraints. In the event of a tie, the model with the highest DockQ score was selected. If a reference structure was unavailable, we defaulted to the first generated model among the tied candidates. The average percentage of satisfied constraints across all 5 generated samples is also indicated together with the standard deviation. Bold values highlight a substantial improvement over the baseline model.

Case	Model	Best of 5: Constraints satisfied (%)		Best of 5: Comparison to reference			Avg-5: Constraints satisfied (%)	
		HDX-MS	XL-MS	DockQ \uparrow	iRMSD (\AA , \downarrow)	iRMSD (\AA , \downarrow)	HDX-MS	XL-MS
BRD4-CRBN	Unguided	20	-	0.09 (Incorrect)	20.3	9	20	-
	HDX-MS	100	-	0.28 (Acceptable)	6.5	3	92 \pm 16	-
WDR5-DCAFI	Unguided	-	25	0.05 (Incorrect)	26.7	10.9	-	20 \pm 11.2
	XL-MS	-	100	0.44 (Acceptable)	6.3	2	-	82.6 \pm 11.2
KAT6-CRBN	Unguided	40	63	<i>-no available reference-</i>			40	51 \pm 8.9
	HDX-MS	70	50				68 \pm 4.2	49 \pm 3.8
	XL-MS	60	88				50 \pm 6.7	83 \pm 6.7
	HDX-MS + XL-MS	70	88				67 \pm 4.8	84 \pm 6.3
PTPN2-CRBN	Unguided	0	-	0.03 (Incorrect)	31.5	20.0	0	-
	HDX-MS	50	-	0.31 (Acceptable)	7.0	3.6	40 \pm 20	-
PD1-Nivolumab	Unguided	0	0	0.21 (Incorrect)	68.3	28	0	0
	HDX-MS	100	100	0.58 (Medium)	4.4	2.3	78 \pm 5.8	80 \pm 17.1
	HDX-MS + XL-MS	100	100	0.70 (Medium)	3.4	1.6	100	100

4.1 Experimental setup and data curation

For the synthetic benchmarks, we curated a set of protein complexes, including PROTAC ternary complexes and protein-antibody complexes, from the Protein Data Bank (PDB). We selected structures deposited after June 1, 2023 to ensure they were excluded from the Boltz-2 training set to prevent data leakage. Using these ground-truth structures, we simulated both XL-MS and HDX-MS data. Synthetic cross-links were generated by identifying target residue pairs (e.g., Lysine-Lysine) that fall within a strictly defined spatial threshold, accurately mimicking physical cross-linker arm lengths. Synthetic HDX-MS protection factors were derived by calculating the theoretical Solvent Accessible Surface Area (SASA) directly from the experimental coordinates. For our experimental evaluations,

we utilized processed XL-MS and HDX-MS data, combining datasets curated from the literature with novel data generated in-house. We then translated these discrete experimental measurements into continuous distance constraints and surface protection patterns.

To evaluate experimental agreement and structural integrity of our models, we utilize a number of metrics to capture both global agreement and local satisfaction of constraints. When a ground-truth structure is available, we assess docking accuracy using DockQ[33]. For highly dynamic complexes, such as PROTAC induced ternary structures, DockQ might be misleading, therefore we also report Ligand Root Mean Square Deviation (lRMSD) and Interface Root Mean Square Deviation (iRMSD) to provide a general view of the structural accuracy. To evaluate the protection patterns of proteins, we calculate the change in the Relative Solvent Accessible Surface Area (Δ RSA), which divides the absolute SASA by the maximum SASA for each amino acid[34]. We assess the change in protection by calculating the RSA difference between the monomeric and complex states. Satisfaction of an HDX-MS constraint was defined as Δ RSA \geq 0.05 (higher delta means more protection). The overall score is the percentage of constrained residues meeting this threshold. For XL-MS data, we calculate the Euclidean distance between the C α atoms of each pair of residues. Thresholds for satisfaction were set based on the cross-linker type. For positive constraints, satisfaction is when the measured distance is less-than or equal to the threshold, while negative constraint satisfaction is when the measured distance is larger than the defined threshold. We evaluate overall satisfaction as the percentage of pairs that meet their respective thresholds.

The prediction tasks were run on an AWS EC2 g5.8xlarge instance, with 32vCPUs, 64GiB RAM, and NVIDIA A10G GPU.

4.2 Performance on synthetic MS data

BRD4-PROTAC-CRBN. The ternary structure of BRD4-CRBN was shown to adopt distinct conformations depending on PROTAC used. While earlier crystal structures such as PDB: 6BOY (with the dBET6 PROTAC) established a specific conformation[8], a more recent crystal structure, PDB: 8RQ9, confirmed that CFT1297 stabilizes a different conformation[35]. Despite the experimental evidence, Boltz-2 defaults the prediction with CFT1297 to the wrong PDB: 6BOY pose. We created synthetic HDX-MS data based on the difference between the two crystal structures (6BOY vs. 8RQ9). Using 5 residues as constraints that were chosen by the constraints subsetting algorithm, the model was able to predict the correct ternary orientation with satisfaction of all of the HDX-MS constraints. The guidance improved the lRMSD from 20.3 Å to 6.5 Å (Table 1 and Figure S2).

WDR5-PROTAC-DCAF1. Recent structural data demonstrates that active and inactive PROTACs induce distinctly different orientations of WDR5 relative to DCAF1[36]. We found that Boltz-2 fails to capture this activity-dependent shift, incorrectly defaulting to an inactive conformation even when tasked with predicting an active ternary complex (Figure S1). While applying either positive or negative constraints improved the performance of the model, guiding the prediction with a combination of both yielded the best scores and successfully rescued the active target state, driving the iRMSD down from 10.9 Å to 2 Å (Figure S1).

4.3 Performance on experimental MS data

KAT6A-PROTAC-CRBN. Since this complex lacks solved experimental structures, we generated in house HDX-MS and XL-MS data, differentiating between active and inactive compounds, to steer our model toward the productive conformation. We found that using HDX-MS constraints alone successfully satisfies the local protection data, improving the HDX-MS satisfaction of the best prediction from 40% to 70%, but does not improve the global XL-MS fit (Table 1). Guiding our model with XL-MS constraints alone improves satisfaction of both sets of data. Layering both HDX-MS and XL-MS together best satisfies the constraints with the top model fulfilling 70% of the HDX-MS and 88% of the XL-MS constraints, an improvement that holds up consistently across the 5-model averages.

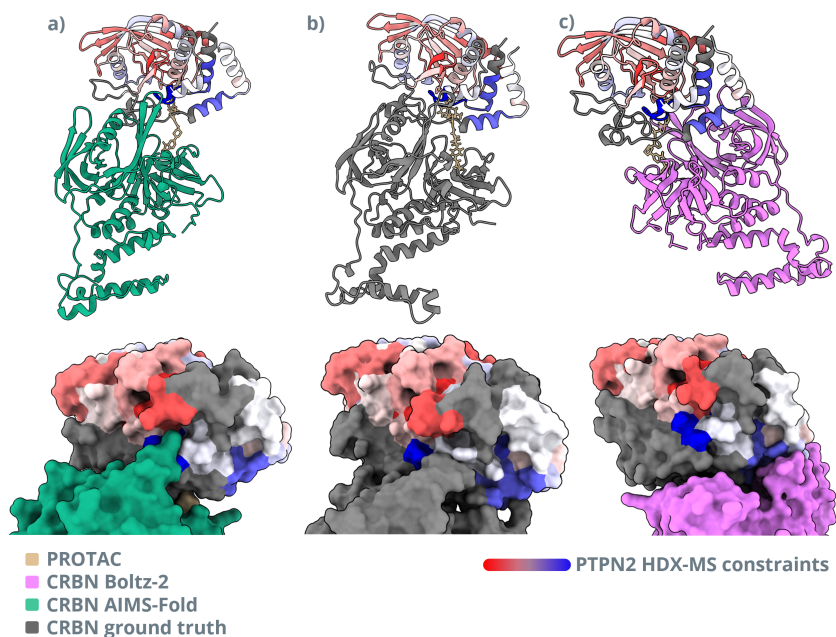


Figure 2: PTPN2-PROTAC-CRBN co-folding. (a) AIMS-Fold predicted conformation partially agrees with the HDX-MS data. (b) The ground truth selected is cryo-EM initialized MD simulation frame that best agrees with HDX-MS data. (c) Boltz-2 predicts an incorrect conformation that doesn't agree the experimental data.

PTPN2-PROTAC-CRBN. We used the cryo-EM ternary complex (PDB: 8UH6) as a starting structural model. Static cryo-EM structures do not always capture intrinsic protein flexibility in solution, leading to discrepancies with solution-phase HDX-MS data. Since the investigators from [37] note substantial flexibility of the complex and low agreement between cryo-EM and HDX-MS data, they performed MD simulations to resolve the discrepancies. We evaluated several frames to identify the most representative one, by screening for the frame that satisfied the highest number of HDX-MS protected residues (defining a residue as protected if its Buried Surface Area was $> 5 \text{ \AA}^2$). This best-fit frame served as the reference for the quantitative benchmarks, including DockQ, IRMSD, and iRMSD calculations.

While an unguided Boltz-2 prediction failed to capture the correct orientation ($iRMSD = 19.8 \text{ \AA}$), AIMS-Fold successfully utilized the HDX-MS constraints to find the correct conformation, yielding an iRMSD of 3.6 \AA against the selected reference frame (Figure 2, Table 1). However, as noted in Figure 2a and Table 1, the guided model satisfies only 50% of constraints, highlighting a strong inherent training bias that resists extreme conformational shifts, and a specific area for future refinement.

PD-1-Nivolumab. Nivolumab is a cornerstone of cancer immunotherapy that functions by binding to the Programmed Cell Death Protein 1 (PD-1), preventing the deactivation of the host immune response. Boltz-2 fails to accurately predict the binding interface between the two, incorrectly positioning PD-1 on the wrong side of the Nivolumab (Figure 3). These spatial errors result in poor DockQ and high iRMSD and IRMSD values when comparing to the crystal structure (PDB: 5WT9, Table 1), underscoring the complexity of antibody-antigen complex predictions.

To address this, we derived HDX-MS constraint subsets (as described in Methods Section 3.4), from previously published data, as well as XL-MS constraints[38]. While one out of the five HDX-MS guided prediction models satisfied all of the constraints, incorporation of both HDX-MS and XL-MS

data refined the modeling to satisfy 100% of the constraints in all 5 generated models, with DockQ scores reaching up to 0.70 and iRMSD values of 1.6 Å (Table 1 and Figures S3, S4).

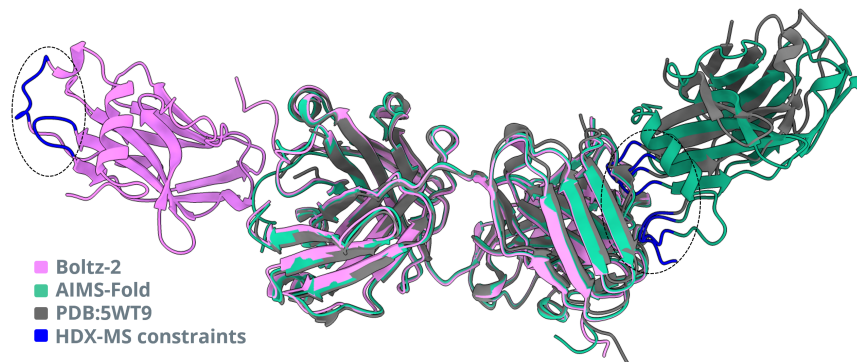


Figure 3: PD-1-Nivolumab co-folding. The guided model covers the right interface area specified in the HDX-MS data and agrees with the crystal structure. The unconstrained model on the other hand places the interface on the opposite side.

4.4 Guided generation vs. Post-hoc filtering

The default strategy for integrating experimental data into computational modeling was to use structural constraints to score and filter a large ensemble of naive predictions post-generation. However, this post-hoc filtering strategy relies on the assumption that the unconstrained generative model actually sampled the correct conformation. In vast and highly flexible conformational spaces, such as PROTAC ternary structures, unconstrained models can collapse into global energy minima or static states memorized during training. If the model never explores the specific structural basin indicated by the proteomics data, generating and filtering thousands of decoy models will simply yield invalid results. To overcome this fundamental limitation, guided generation is required. Rather than passively relying on stochastic sampling to stumble upon the correct structure, inference-time steering actively alters the probability landscape throughout the generation process into biologically valid conformational basins that satisfy the experimental constraints.

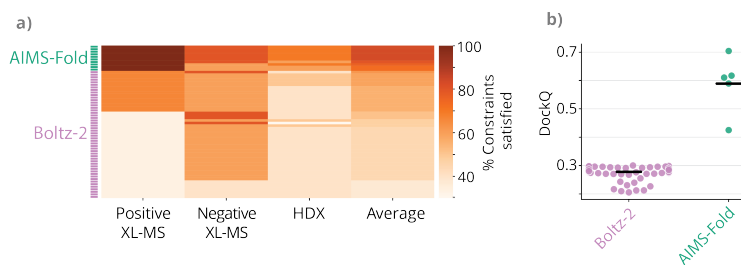


Figure 4: Post-hoc filtering is insufficient for the detection of the correct conformation. (A) For the KAT6A-PROTAC-CRBN complex, 10 guided models are compared to 50 Boltz-2 predictions across 5 different seeds. Rows represent models, columns represent constraint type and color indicates % constraints fulfilled. The models are sorted based on the average % constraints satisfied. All naive models are ranked below the 10 guided ones. (B) Swarm plot of DockQ scores for the PD1-Nivolumab complex, comparing 5 guided AIMS-Fold models against 100 naive Boltz-2 predictions, generated across 10 different seeds, evaluated against the ground-truth Cryo-EM structure.

To demonstrate this, we compared 10 KAT6A-PROTAC-CRBN predictions generated by our model against 50 unguided predictions generated by Boltz-2 across 5 different random seeds. These models were ranked based on their average satisfaction across three experimental constraints: positive XL-

MS, negative XL-MS, and HDX-MS. Ranking the generated structures by constraint satisfaction revealed that the 10 guided models were ranked at the top 10 positions, clearly outperforming all 50 unconstrained predictions (Figure 4A). However, because no ground-truth experimental structure exists for the KAT6A ternary complex, and constraint satisfaction alone cannot definitively prove structural accuracy, we sought to confirm this fundamental limitation of unguided generation against a known structural reference. Returning to the PD1-Nivolumab complex, where our guided models successfully captured the Cryo-EM conformation, we tested whether extensive unguided sampling could eventually stumble upon the correct state. We generated 100 unguided Boltz-2 predictions across 10 independent seeds. Consistent with the KAT6A results, the naive model completely failed to sample the correct structural basin, as the 5 AIMS-Fold models scored substantially higher than all 100 unguided predictions (Figure 4B).

5 Discussion

In this work, we introduced AIMS-Fold, demonstrating the first systematic approach to combining structural proteomics and diffusion-based AI models for protein structure solving, enabling rational drug design. Across our benchmarks, AIMS-Fold significantly increased structural prediction accuracy for highly flexible, induced proximity and antibody based systems. Crucially, we demonstrated that unconstrained AI models, such as Boltz-2, predict static states that are heavily biased by their PDB training distributions[13, 39]. Consequently, they can overlook biologically active conformations[40]. By actively steering the generative trajectory, the model successfully identifies these overlooked conformations. Furthermore, we showed that XL-MS and HDX-MS can provide complementary constraints[1].

The implications of this framework for rational drug design, particularly for PROTACs and molecular glues, are profound as their efficacy is driven by the dynamic assembly of a ternary complex (e.g., POI-E3-PROTAC) rather than binary affinity of the compound to the protein[2, 8]. Traditional experimental approaches, such as X-ray crystallography and Cryo-EM, are low-throughput, costly, and static, freezing the dynamics of the complex[41, 1]. Equivalently, computational methods like molecular docking or molecular dynamics suffer from insufficient sampling and high computational costs[42, 43].

AIMS-Fold overcomes these limitations by utilizing MS data to capture proteins in their native, dynamic states at a higher throughput. For instance, in the rational design of PROTACs, it is well established that even minor modifications to a linker can completely obliterate target degradation by altering ternary complex cooperativity and by disrupting the ubiquitination zone[8]. Standard, unconstrained AI prediction models fail to capture these subtle structural modifications, while AIMS-Fold accurately models these PROTAC-dependent conformational shifts.

Despite these advancements, our approach has notable limitations regarding both experimental data acquisition and the underlying computational model. Experimentally, AIMS-Fold is constrained by MS peptide affinity and sequence coverage. XL-MS applicability heavily depends on the prevalence and accessibility of specific residues, particularly lysines, at the protein-protein interface[44, 45]. If these residues are absent, XL-MS utilization is restricted. Furthermore, XL-MS requires the cross-linked residues to fall strictly within a restrictive spatial distance (typically $< 30 \text{ \AA}$)[17]. Similarly, HDX-MS is limited by peptide-level sequence coverage and resolution[46]. Because HDX-MS yields peptide-level resolution instead of atomic level, it can introduce noise into the guidance gradients, as protection patterns might be affected by adjacent residues rather than direct binding ones and the other way around. Computationally, AIMS-Fold remains inherently limited by the training weights and biases of the base Boltz architecture. If the experimental MS data points to a conformational state that deviates too extremely from the model's training data, the underlying neural network can sometimes resist the applied steering potentials, leading to suboptimal constraint satisfaction. Lastly, it is important to note that while AIMS-Fold is potentially more accurate than Boltz-2, it requires the generation of complex experimental data which may not always be feasible.

Mitigating these limitations will be the focus of future research. The reliance on lysine-specific cross-linking can be addressed by incorporating orthogonal chemistries that target acidic residues or provide non-specific mapping[16, 47]. Computationally, while the current iteration of AIMS-Fold generates highly accurate singular structures, the comprehensive understanding of ternary complexes requires exploring broad conformational ensembles. In future work, we aim to leverage the continuous and dynamic nature of HDX-MS data to reveal multiple distinct, dynamic conformations of these complexes.

6 Declaration of Interests

All authors are employees and shareholders of Protai Bio, Ramat Gan, Israel

References

- [1] Miklós Békés, David R Langley, and Craig M Crews. PROTAC targeted protein degraders: the past is prologue. *Nat Rev Drug Discov*, 21(3):181–200, March 2022.
- [2] Stuart L Schreiber. The rise of molecular glues. *Cell*, 184(1):3–9, January 2021.
- [3] Jake A Ward, Carles Perez-Lopez, and Cristina Mayor-Ruiz. Biophysical and computational approaches to study ternary complexes: A ‘cooperative relationship’ to rationalize targeted protein degradation. *Chembiochem*, 24(10):e202300163, May 2023.
- [4] Ryan P Wurz, Huan Rui, Ken Dellamaggiore, Sudipa Ghimire-Rijal, Kaylee Choi, Kate Smither, Albert Amegadzie, Ning Chen, Xiaofen Li, Abhisek Banerjee, Qing Chen, Dane Mohl, and Amit Vaish. Affinity and cooperativity modulate ternary complex formation to drive targeted protein degradation. *Nat. Commun.*, 14(1):4177, July 2023.
- [5] Huan Rui, Kate S Ashton, Jaeki Min, Connie Wang, and Patrick Ryan Potts. Protein-protein interfaces in molecular glue-induced ternary complexes: classification, characterization, and prediction. *RSC Chem. Biol.*, 4(3):192–215, March 2023.
- [6] Scott J Hughes and Alessio Ciulli. Molecular recognition of ternary complexes: a new dimension in the structure-guided design of chemical degraders. *Essays Biochem.*, 61(5):505–516, November 2017.
- [7] Mikhail Ignatov, Akhil Jindal, Sergei Kotelnikov, Dmitri Beglov, Ganna Posternak, Xiaojing Tang, Pierre Maisonneuve, Gennady Poda, Robert A Batey, Frank Sicheri, Adrian Whitty, Peter J Tonge, Sandor Vajda, and Dima Kozakov. High accuracy prediction of PROTAC complex structures. *J. Am. Chem. Soc.*, 145(13):7123–7135, April 2023.
- [8] Radosław P Nowak, Stephen L DeAngelo, Dennis Buckley, Zhixiang He, Katherine A Donovan, Jian An, Nozhat Safae, Mark P Jedrychowski, Charles M Ponthier, Mette Ishoey, Tinghu Zhang, Joseph D Mancias, Nathanael S Gray, James E Bradner, and Eric S Fischer. Plasticity in binding confers selectivity in ligand-induced protein degradation. *Nat Chem Biol*, 14(7):706–714, July 2018.
- [9] Philip P Chamberlain and Lawrence G Hamann. Development of targeted protein degradation therapeutics. *Nat Chem Biol*, 15(10):937–944, October 2019.
- [10] Josh Abramson, Jonas Adler, Jack Dunger, Richard Evans, Tim Green, Alexander Pritzel, Olaf Ronneberger, Lindsay Willmore, Andrew J Ballard, Joshua Bambrick, Sebastian W Bodenstein, David A Evans, Chia-Chun Hung, Michael O’Neill, David Reiman, Kathryn Tunyasuvunakool, Zachary Wu, Akvilė Žemgulytė, Eirini Arvaniti, Charles Beattie, Ottavia Bertolli, Alex Bridgland, Alexey Cherepanov, Miles Congreve, Alexander I Cowen-Rivers, Andrew Cowie, Michael Figurnov, Fabian B Fuchs, Hannah Gladman, Rishub Jain, Yousuf A Khan, Caroline M R Low, Kuba Perlin, Anna Potapenko, Pascal Savy, Sukhdeep Singh, Adrian

- Stecula, Ashok Thillaisundaram, Catherine Tong, Sergei Yakneen, Ellen D Zhong, Michal Zielinski, Augustin Židek, Victor Bapst, Pushmeet Kohli, Max Jaderberg, Demis Hassabis, and John M Jumper. Accurate structure prediction of biomolecular interactions with AlphaFold 3. *Nature*, 630(8016):493–500, June 2024.
- [11] Saro Passaro, Gabriele Corso, Jeremy Wohlwend, Mateo Reveiz, Stephan Thaler, Vignesh Ram Somnath, Noah Getz, Tally Portnoi, Julien Roy, Hannes Stark, David Kwabi-Addo, Dominique Beaini, Tommi Jaakkola, and Regina Barzilay. Boltz-2: Towards accurate and efficient binding affinity prediction. June 2025.
- [12] Khoa Ngo, Pei-Chi Yang, Vladimir Yarov-Yarovoy, Colleen E Clancy, and Igor Vorobyov. Harnessing AlphaFold to reveal hERG channel conformational state secrets. *Elife*, 13(RP104901): RP104901, July 2025.
- [13] Thomas J Lane. Protein structure prediction has reached the single-structure frontier. *Nat Methods*, 20(2):170–173, February 2023.
- [14] Gilberto P Pereira, Corentin Gouzien, Paulo C T Souza, and Juliette Martin. Challenges in predicting PROTAC-mediated protein-protein interfaces with AlphaFold reveal a general limitation on small interfaces. *Bioinform. Adv.*, 5(1):vbaf056, March 2025.
- [15] Nils Dunlop, Francisco Erazo, Farzaneh Jalalypour, and Rocío Mercado. Predicting PROTAC-mediated ternary complexes with AlphaFold3 and boltz-1. *Digit. Discov.*, 4(12):3782–3809, 2025.
- [16] Kitaik Lee and Francis J O’Reilly. Cross-linking mass spectrometry for mapping protein complex topologies in situ. *Essays Biochem*, 67(2):215–228, March 2023.
- [17] Glenn R Masson, John E Burke, Natalie G Ahn, Ganesh S Anand, Christoph Borchers, Sébastien Brier, George M Bou-Assaf, John R Engen, S Walter Englander, Johan Faber, Rachel Garlish, Patrick R Griffin, Michael L Gross, Miklos Guttman, Yoshitomo Hamuro, Albert J R Heck, Damian Houde, Roxana E Iacob, Thomas J D Jørgensen, Igor A Kaltashov, Judith P Klinman, Lars Konermann, Petr Man, Leland Mayne, Bruce D Pascal, Dana Reichmann, Mark Skehel, Joost Snijder, Timothy S Strutzenberg, Eric S Underbakke, Cornelia Wagner, Thomas E Wales, Benjamin T Walters, David D Weis, Derek J Wilson, Patrick L Wintrode, Zhongqi Zhang, Jie Zheng, David C Schriemer, and Kasper D Rand. Recommendations for performing, interpreting and reporting hydrogen deuterium exchange mass spectrometry (HDX-MS) experiments. *Nat Methods*, 16(7):595–602, July 2019.
- [18] Yanbin Wang and Ming Chen. Extrapolating foundation generative models with physics: A case study of exploring peptide conformations under protein-environment interactions. *J. Phys. Chem. Lett.*, 17(2):456–465, January 2026.
- [19] Liyao Wang, Andrejs Tučs, Songting Ding, Koji Tsuda, and Adnan Sljoka. HDXRank: A deep learning framework for ranking protein complex predictions with hydrogen-deuterium exchange data. *J. Chem. Theory Comput.*, 21(14):7173–7187, July 2025.
- [20] Minh H Tran, Cristina E Martina, Rocco Moretti, Marcus Nagel, Kevin L Schey, and Jens Meiler. RosettaHDX: Predicting antibody-antigen interaction from hydrogen-deuterium exchange mass spectrometry data. *J. Struct. Biol.*, 217(1):108166, March 2025.
- [21] Victoria A Roberts, Elaine E Thompson, Michael E Pique, Martin S Perez, and L F Ten Eyck. DOT2: Macromolecular docking with improved biophysical models. *J. Comput. Chem.*, 34(20): 1743–1758, July 2013.
- [22] Hyungjin Chung, Jeongsol Kim, Michael T Mccann, Marc L Klasky, and Jong Chul Ye. Diffusion posterior sampling for general noisy inverse problems. May 2024.

- [23] Yang Song, Jascha Sohl-Dickstein, Diederik P Kingma, Abhishek Kumar, Stefano Ermon, and Ben Poole. Score-based generative modeling through stochastic differential equations. November 2020.
- [24] Brian D O Anderson. Reverse-time diffusion equation models. *Stoch. Process. Their Appl.*, 12(3):313–326, May 1982.
- [25] Pascal Vincent. A connection between score matching and denoising autoencoders. *Neural Comput*, 23(7):1661–1674, July 2011.
- [26] Bradley Efron. Tweedie’s formula and selection bias. *J Am Stat Assoc*, 106(496):1602–1614, 2011.
- [27] Jianyu Zhang, Jeremy L Balsbaugh, Shuaihua Gao, Natalie G Ahn, and Judith P Klinman. Hydrogen deuterium exchange defines catalytically linked regions of protein flexibility in the catechol o-methyltransferase reaction. *Proc. Natl. Acad. Sci. U. S. A.*, 117(20):10797–10805, May 2020.
- [28] Cyril Dominguez, Rolf Boelens, and Alexandre M J J Bonvin. HADDOCK: a protein-protein docking approach based on biochemical or biophysical information. *J Am Chem Soc*, 125(7):1731–1737, February 2003.
- [29] Michael P Rout and Andrej Sali. Principles for integrative structural biology studies. *Cell*, 177(6):1384–1403, May 2019.
- [30] Kolja Stahl, Andrea Graziadei, Therese Dau, Oliver Brock, and Juri Rappsilber. Protein structure prediction with in-cell photo-crosslinking mass spectrometry and deep learning. *Nat Biotechnol*, 41(12):1810–1819, December 2023.
- [31] Kolja Stahl, Robert Warneke, Lorenz Demann, Rica Bremenkamp, Björn Hormes, Oliver Brock, Jörg Stülke, and Juri Rappsilber. Modelling protein complexes with crosslinking mass spectrometry and deep learning. *Nat Commun*, 15(1):7866, September 2024.
- [32] Rishwanth Raghu, Axel Levy, Gordon Wetzstein, and Ellen D Zhong. Multiscale guidance of protein structure prediction with heterogeneous cryo-EM data. December 2025.
- [33] Sankar Basu and Björn Wallner. DockQ: A quality measure for Protein-Protein docking models. *PLOS ONE*, 11(8):e0161879, August 2016.
- [34] Matthew Z Tien, Austin G Meyer, Dariya K Sydykova, Stephanie J Spielman, and Claus O Wilke. Maximum allowed solvent accessibilities of residues in proteins. *PLoS One*, 8(11):e80635, November 2013.
- [35] Alena Kroupova, Valentina A Spiteri, Zoe J Rutter, Hirotake Furihata, Darren Darren, Sarath Ramachandran, Sohini Chakraborti, Kevin Haubrich, Julie Pethe, Denzel Gonzales, Andre J Wijaya, Maria Rodriguez-Rios, Manon Sturbaut, Dylan M Lynch, William Farnaby, Mark A Nakasone, David Zollman, and Alessio Ciulli. Design of a cereblon construct for crystallographic and biophysical studies of protein degraders. *Nature Communications*, 15(1):8885, October 2024.
- [36] Mark F Mabanglo, Brian Wilson, Mahmoud Nouredin, Serah W Kimani, Ahmed Mamai, Chiara Krausser, Héctor González-Álvarez, Smriti Srivastava, Mohammed Mohammed, Laurent Hoffer, Manuel Chan, Jamie Avrumutsoae, Alice Shi Ming Li, Taraneh Hajian, Sarah Tucker, Stuart Green, Magdalena Szewczyk, Dalia Barsyte-Lovejoy, Vijayaratnam Santhakumar, Suzanne Ackloo, Peter Loppnau, Yanjun Li, Almagul Seitova, Taira Kiyota, Jue George Wang, Gilbert G Privé, Douglas A Kuntz, Bhashant Patel, Vaibhavi Rathod, Anand Vala, Bhimsen Rout, Ahmed Aman, Gennady Poda, David Uehling, Jailall Ramnauth, Levon Halabelian, Richard Marcellus, Rima Al-Awar, and Masoud Vedadi. Crystal structures of DCAF1-PROTAC-WDR5 ternary complexes provide insight into DCAF1 substrate specificity. *Nat Commun*, 15(1):10165, November 2024.

- [37] Qi Hao, Manoj K Rathinaswamy, Kelly L Klinge, Matthew Bratkowski, Amirhossein Mafi, Christina K Baumgartner, Keith M Hamel, Gesine K Veits, Rinku Jain, Claudio Catalano, Mark Fitzgerald, Alexander W Hird, Eunice Park, Harit U Vora, James A Henderson, Kenton Longenecker, Charles W Hutchins, Wei Qiu, Giovanna Scapin, Qi Sun, Vincent S Stoll, Chaohong Sun, Ping Li, Dan Eaton, David Stokoe, Stewart L Fisher, Christopher G Nasveschuk, Marcia Paddock, and Michael E Kort. Mechanistic insights into a heterobifunctional degrader-induced PTPN2/N1 complex. *Commun Chem*, 7(1):183, August 2024.
- [38] Mengru Mira Zhang, Richard Y-C Huang, Brett R Beno, Ekaterina G Deyanova, Jing Li, Guodong Chen, and Michael L Gross. Epitope and paratope mapping of PD-1/Nivolumab by mass Spectrometry-Based Hydrogen-Deuterium exchange, cross-linking, and molecular docking. *Analytical Chemistry*, May 2020.
- [39] Tadeo Saldaño, Nahuel Escobedo, Julia Marchetti, Diego Javier Zea, Juan Mac Donagh, Ana Julia Velez Rueda, Eduardo Gonik, Agustina García Melani, Julieta Novomisky Nechcoff, Martín N Salas, Tomás Peters, Nicolás Demitroff, Sebastian Fernandez Alberti, Nicolas Palopoli, Maria Silvina Fornasari, and Gustavo Parisi. Impact of protein conformational diversity on AlphaFold predictions. *Bioinformatics*, 38(10):2742–2748, April 2022.
- [40] Hannah K Wayment-Steele, Adedolapo Ojoawo, Renee Otten, Julia M Apitz, Warintra Pitsawong, Marc Hömberger, Sergey Ovchinnikov, Lucy Colwell, and Dorothee Kern. Predicting multiple conformations via sequence clustering and AlphaFold2. *Nature*, 625(7996):832–839, January 2024.
- [41] Morgan S Gadd, Andrea Testa, Xavier Lucas, Kwok-Ho Chan, Wenzhang Chen, Douglas J Lamont, Michael Zengerle, and Alessio Ciulli. Structural basis of PROTAC cooperative recognition for selective protein degradation. *Nat Chem Biol*, 13(5):514–521, May 2017.
- [42] Michael L Drummond and Christopher I Williams. In silico modeling of PROTAC-Mediated ternary complexes: Validation and application. *J Chem Inf Model*, 59(4):1634–1644, April 2019.
- [43] Gaoqi Weng, Junbo Gao, Zhe Wang, Ercheng Wang, Xueping Hu, Xiaojun Yao, Dongsheng Cao, and Tingjun Hou. Comprehensive evaluation of fourteen docking programs on Protein-Peptide complexes. *J Chem Theory Comput*, 16(6):3959–3969, June 2020.
- [44] Xiaoyun Zhang, Jian-Hua Wang, Dan Tan, Qiang Li, Maodong Li, Zhou Gong, Chun Tang, Zhirong Liu, Meng-Qiu Dong, and Xiaoguang Lei. Carboxylate-selective chemical cross-linkers for mass spectrometric analysis of protein structures. *Anal. Chem.*, 90(2):1195–1201, January 2018.
- [45] Beirong Zhang, Zhou Gong, Bowen Zhong, Zhen Liang, Yukui Zhang, Qun Zhao, and Lihua Zhang. Ultrafiltration-enhanced cross-linking mass spectrometry for comprehensive analysis of low molecular weight protein cross-links. *Anal. Chem.*, 97(18):9606–9612, May 2025.
- [46] Weronika Puchała, Michał Kistowski, Liliya Zhukova, Michał Burdukiewicz, and Michał Dadlez. HRaDeX: R package and web server for computing high-resolution deuterium uptake rates for HDX-MS data. *J. Proteome Res.*, 24(4):1688–1700, April 2025.
- [47] Francis J O’Reilly and Juri Rappsilber. Cross-linking mass spectrometry: methods and applications in structural, molecular and systems biology. *Nat. Struct. Mol. Biol.*, 25(11):1000–1008, November 2018.

A Supplemental background

A.1 Distance and contact constraints in Boltz-2

To allow extended user control over the generated structures, Boltz-2 introduced contact and pocket conditioning, allowing users to specify distance constraints derived from experimental methods or expert knowledge[11]. For a specified pair of atoms i and j , the experimental constraint defines an allowable distance range $[d_{\min}, d_{\max}]$. At a given diffusion timestep, the Euclidean distance d_{ij} is calculated from the predicted denoised coordinates $\hat{\mathbf{x}}_0(\mathbf{x}, t)$. Boltz-2 applies a flat-bottomed distance potential U_{dist} , formulated as a quadratic penalty on boundary violations:

$$U_{\text{dist}}(\mathbf{x}) = \sum_{(i,j)} (\max(0, d_{ij} - d_{\max})^2 + \max(0, d_{\min} - d_{ij})^2) \quad (1)$$

If d_{ij} falls outside the allowed bounds, $\nabla_{\mathbf{x}}U_{\text{dist}}$ yields a non-zero gradient. During the reverse sampling process, this gradient continuously pushes or pulls the specified coordinates. This mechanism forms the mathematical foundation necessary to integrate sparse spatial proteomics data, such as XL-MS, actively steering the global topology of the complex until the distance requirements are satisfied.

B Supplemental methods

B.1 Guidance scheduling

The piecewise timestep schedules are strictly defined over the reverse diffusion trajectory bounded by $t = 1$, representing pure noise, and $t = 0$, representing the fully denoised structure. For the hydrogen-deuterium exchange guidance, the potential is evaluated at every diffusion step, corresponding to an interval of 1. Continuous evaluation was implemented in this framework to prevent the structure from prematurely committing to specific conformations, ensuring the gradient could intervene effectively before the sampling trajectory became fixed. We define a maximum guidance weight of 2, which was empirically escalated from weaker defaults to ensure the computed gradient is forceful enough to compete with the primary diffusion score network. The weight is scaled dynamically across three discrete stages. For $t \in (0.95, 1]$, the guidance is disabled entirely. For $t \in (0.7, 0.95]$, the potential is applied at 25% strength, equating to a weight of 0.5. Finally, for $t \in [0, 0.7]$, the potential is applied at the full strength of 2.0. Associated hyperparameters include a penalty scalar of $k = 20$ and a Gaussian kernel width of $\sigma = 5$. We significantly increased the penalty weight to ensure it was strong enough to actually force protected residues into the core of the protein, preventing it from being overpowered by the main AI model. We also narrowed the search radius to 5.0 Å so the model only counts atoms that are directly next to each other. This gives us a much cleaner signal and prevents the model from being confused by distant atoms while the structure is still messy and forming. Finally, we set the exposure tolerance to zero, meaning that even the slightest bit of surface exposure is strictly penalized. For the cross-linking mass spectrometry spatial guidance, the potential is computed more sparsely at an interval of 4 diffusion steps. The spatial guidance weight follows a distinct three-stage step function where it remains disabled for $t \in (0.75, 1]$. For $t \in (0.25, 0.75]$, the guidance is applied at 50% strength. In the final stages of diffusion, bounded by $t \in [0, 0.25]$, the potential is applied at 100% strength. Additionally, the union lambda parameter for these spatial constraints utilizes an exponential interpolation starting at 8.0 and ending at 0.0 with an alpha of -2.0.

B.2 Constraints derivation from raw data

Cross-linking mass spectrometry constraints are derived directly from normalized, high-confidence MS intensity data. Identified residue pairs are clustered based on their relative cross-link intensities across differential experimental conditions (e.g., active versus inactive proximity-inducing compounds).

Hydrogen-deuterium exchange constraints are derived by comparing the fractional uptake between the ternary complex and the isolated binary or apo states. To estimate individual amino acid uptake, we applied a standard deviation-based peptide filtering protocol. Briefly, individual peptides are excluded if their uptake standard deviation (SD) exceeds 2.5 times the mean peptide SD of the sample. The uptake for a given amino acid is calculated as the weighted mean of all overlapping peptides covering the residue. To translate these uptake values into actionable metrics for structural evaluation, residues are categorized into protection regions (Ternary-Apo protection > 5%) and exposed regions (protection < 5%). For each generated ternary model, the change in solvent-accessible surface area (SASA) upon complex formation is calculated.

C Supplemental results

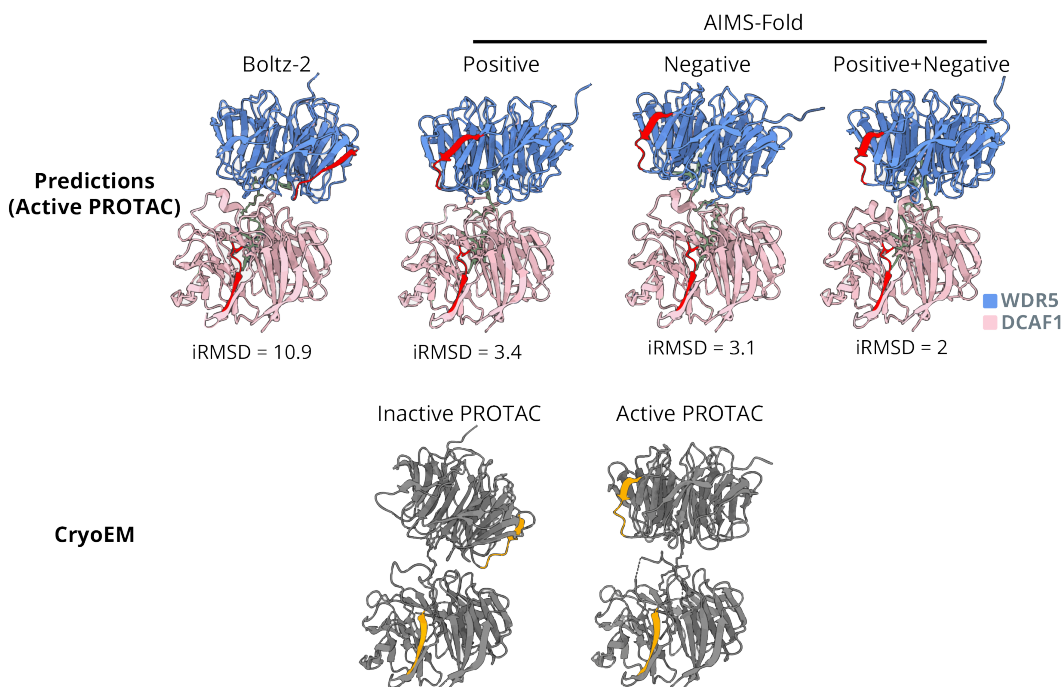


Figure S1: WDR5-PROTAC-DCAF1 co-folding. Using positive and negative XL-MS constraints our model successfully predicts the right orientation of WDR5 relative to DCAF1. All structures are aligned based on DCAF1 with red and orange stretches to visualize the relative rotation of the WDR5.

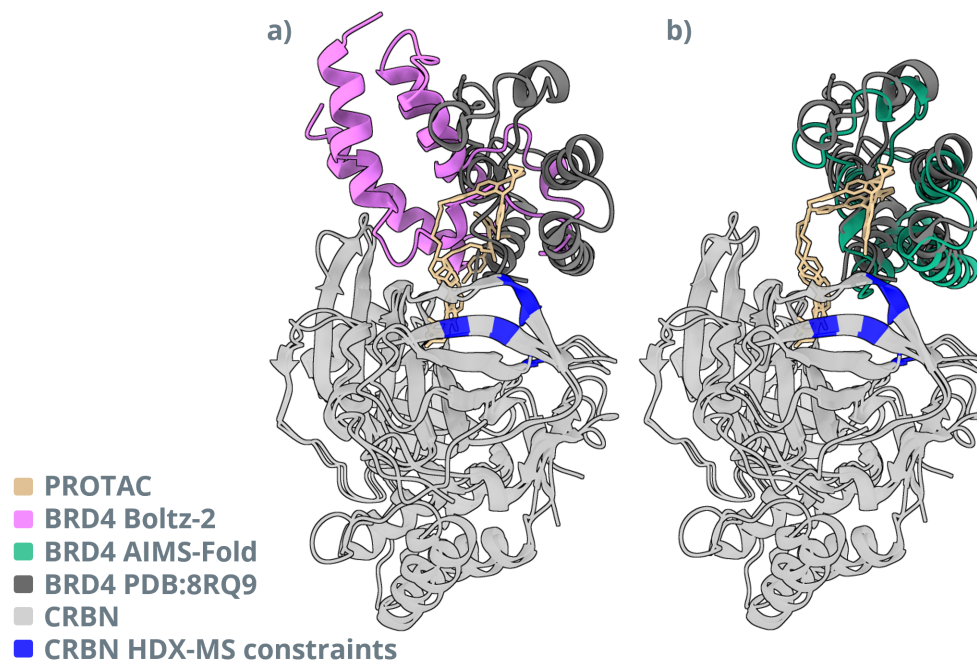


Figure S2: BRD4-PROTAC-CRBN co-folding. a) Boltz-2 predicts a different conformation from the crystal structure, which does not cover protected residues. b) AIMS-Fold predicts the right conformation when guided by HDX-MS data.

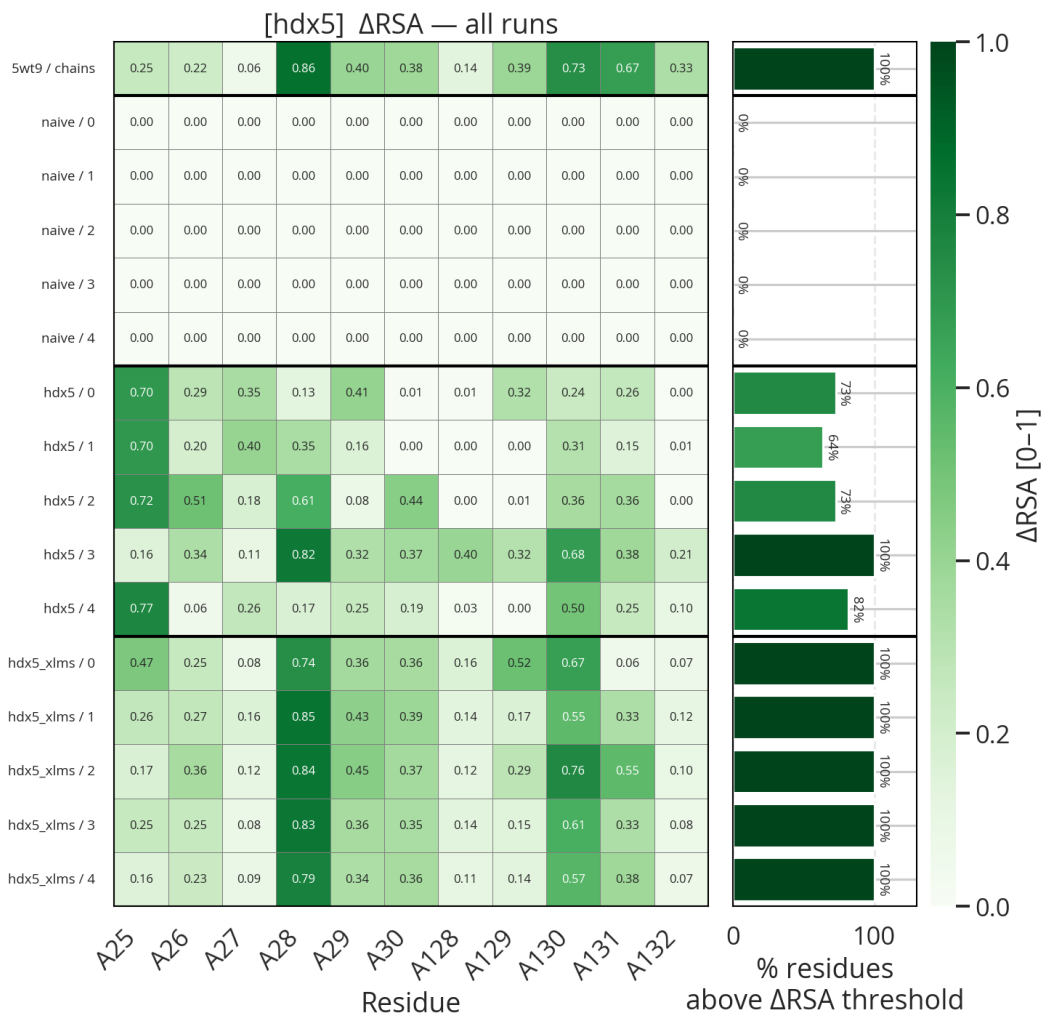


Figure S3: Heatmap detailing the change in Relative Solvent Accessible Surface Area (RSA) across the interaction interface for the PD-1-Nivolumab case, visualizing the HDX-MS protection patterns effectively captured by AIMS-Fold.

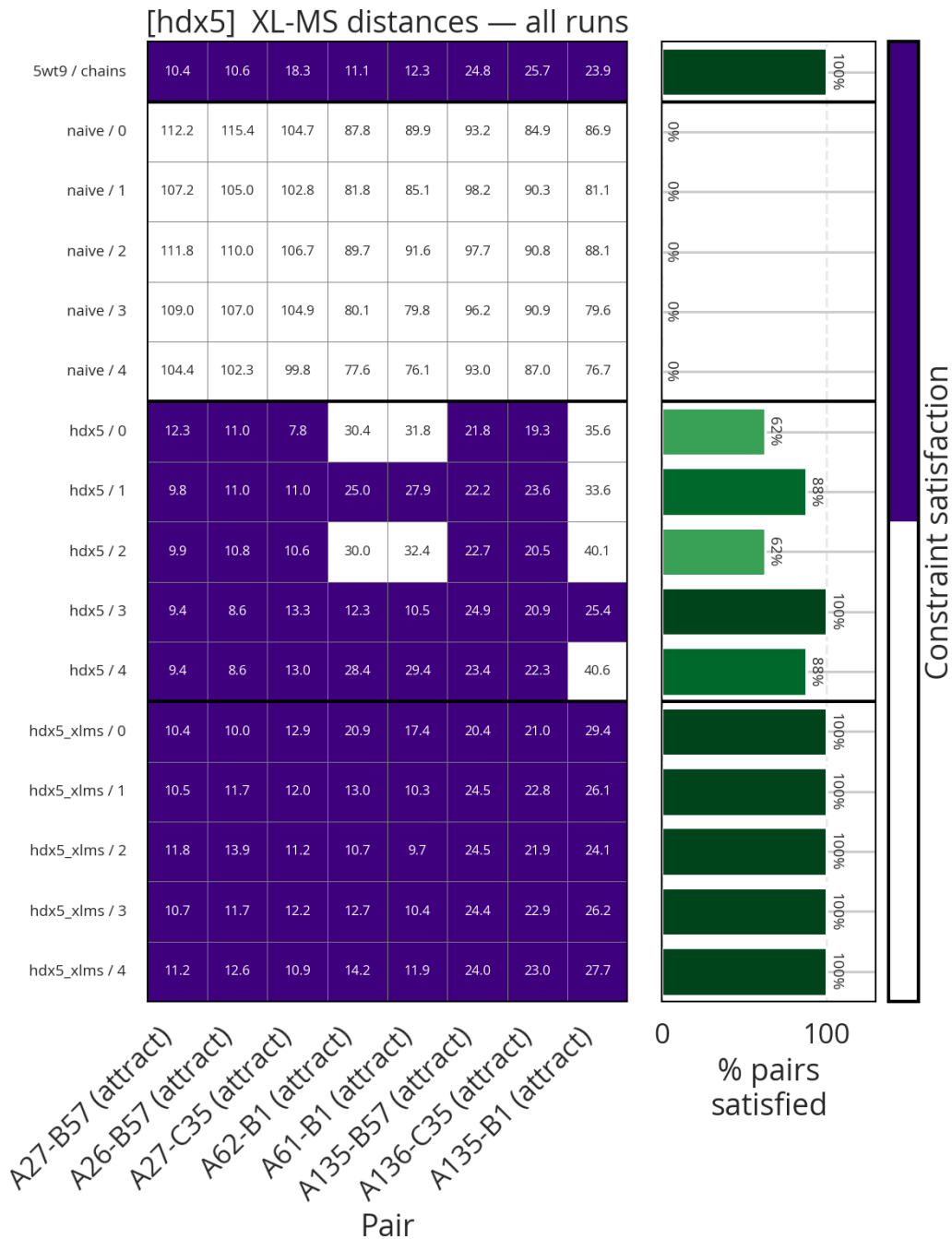


Figure S4: XL-MS distance satisfaction for the best-performing constraint subset in PD-1-Nivolumab case. The guided model successfully pulls cross-linked regions within the physical threshold of the linker, whereas unguided models heavily violate these spatial boundaries.